

Excited-state quantum phase transitions and chaos in a three-level Lipkin model

Alberto Mayorgas*

*Escuela Politécnica Superior, Universidad CEU Fernando III,
CEU Universities, Glorieta Cardenal Herrera Oria, 41930 Sevilla, Spain*

Pedro Pérez-Fernández†

Departamento de Física Aplicada III, Escuela Técnica Superior de Ingeniería, Universidad de Sevilla, 41092 Sevilla, Spain

Álvaro Sáiz‡

*Departamento de Física Aplicada III, Escuela Técnica Superior de Ingeniería,
Universidad de Sevilla, 41092 Sevilla, Spain and
Departamento de Física Atómica, Molecular y Nuclear, Facultad de Física,
Universidad de Sevilla, Apartado 1065, 41080 Sevilla, Spain*

José Miguel Arias§

*Departamento de Física Atómica, Molecular y Nuclear, Facultad de Física,
Universidad de Sevilla, Apartado 1065, 41080 Sevilla, Spain*

(Dated: February 27, 2026)

ABSTRACT

Excited-state quantum phase transitions (ESQPTs) have been extensively studied in two-level models, but their characterization remains challenging in systems displaying mixed regular and chaotic dynamics. In this work, we investigate ESQPTs within the three-level Lipkin–Meshkov–Glick model, where an enlarged Hilbert space and multiple separatrices give rise to rich spectral structures strongly influenced by chaos. To investigate the different dynamical regions, we have calculated Poincaré sections and Peres lattices. In addition, by combining chaos-sensitive measures with standard ESQPT diagnostics, we provide a static analysis of ESQPT signatures in this model and establish a robust framework for future studies of its dynamical behavior. The degree of chaos and the Kullback-Leibler divergence are found to be very effective chaos-sensitive measures, which are complementary to ESQPT diagnostics such as the mean field limit and the participation ratio. Hence we provide a standard framework to work with ESQPTs in chaotic three-level systems.

I. INTRODUCTION

Matter can exist in distinct structural states, or phases, each characterized by specific physical properties. Transitions between phases are accompanied by abrupt changes in these properties. The study of phase transitions and critical phenomena is of fundamental importance because of the emergence of universal behavior largely independent of microscopic details [1, 2].

A phase transition is typically driven by a control parameter—such as temperature or another relevant variable—and characterized by an order parameter that vanishes in one phase and becomes finite in another. The evolution of this order parameter near the transition determines the classification of the phase transition [1, 2].

The concept of phase transitions, originally developed

for macroscopic systems, extends to the quantum domain, giving rise to quantum phase transitions (QPTs) [3–5]. These transitions occur when a control parameter reaches a critical value and have been characterized through various static and dynamic observables. Abrupt variations in ground-state properties define ground-state quantum phase transitions (GSQPTs), whereas singularities in the level density at specific excitation energies mark excited-state quantum phase transitions (ESQPTs) [6]. Such singularities emerge in the thermodynamic limit, where the number of particles tends to infinity, although finite systems display precursor signatures of this critical behavior. Both GSQPTs and ESQPTs have been investigated in numerous two-level models (e.g., Refs. [6–14]).

The objective of this work is to analyze GSQPTs and ESQPTs in a more complex system that exhibits regular, chaotic, and mixed dynamical regimes across different excitation energies. To this end, we employ the three-level Lipkin–Meshkov–Glick (LMG) model as a paradigmatic example [15–18]. The inclusion of a third level increases the spectral complexity and Hilbert-space dimensionality,

* alberto.mayorgasreyes@ceu.es

† pedropf@us.es

‡ asaiz@us.es

§ ariasc@us.es

producing multiple separatrices that partition the spectrum into regions with varying degrees of chaos. Characterizing ESQPTs under such conditions is challenging [13], as the avoided crossings typical of chaotic dynamics interfere with the level clustering associated with ESQPTs [19].

To establish a connection between chaos and ESQPTs, the different possible dynamical regimes—integrable, quasi-integrable, chaotic, and quasi-chaotic—are analyzed by computing Poincaré sections [20] in phase space and Peres lattices [21] for selected observables. In addition, to characterize statically the different regions, we employ measures of chaos and fluctuation—including the nearest-neighbor spacing distribution (NNSD), the degree of chaos η , the Kullback-Leibler divergence, and the overlap distribution [13, 17, 22, 23]—together with conventional ESQPT indicators such as the adjacent-level energy gap, the participation ratio, and the quantum susceptibility. Here, we focus on the static characterization of ESQPTs in the three-level LMG model, leaving the analysis of dynamical aspects for future work.

The paper is organized as follows. Section II introduces the three-level LMG model, the associated parity operators, and the Hilbert space structure. Section III presents the classical limit obtained through an analysis of the energy surface and phase diagram of the system. Section IV discusses the effects of ESQPTs on the regular-to-chaotic transition, including comparisons between Peres lattices and Poincaré sections, NNSD analysis, and the study of susceptibility, the Kullback-Leibler divergence, participation ratio, and overlap distribution. Finally, our conclusions are summarized in Sec. V.

II. MODEL

Many-body Hamiltonians of N identical particles in a D -level system and with infinite-range interactions are usually defined in terms of the $U(D)$ Lie algebra and its associated collective generators S_{ij} , with $i, j = 0, 1, \dots, D-1$, that fulfill the $U(D)$ commutation relations

$$[S_{ij}, S_{kl}] = \delta_{jk} S_{il} - \delta_{il} S_{kj}. \quad (1)$$

It is well known that any arbitrary Lie algebra (as $U(D)$) can be mapped to an oscillator (bosonic) representation using the Jordan-Schwinger transformation. Usually, a realization in terms of bilinear products of boson creation b_i^\dagger and annihilation b_j operators is employed,

$$S_{ij} = b_i^\dagger b_j; \quad i, j = 0, 1, 2, \dots, D-1. \quad (2)$$

For example, in the case of two-level systems $D = 2$ [24–30], the $SU(2)$ angular momentum collective operators are $(J_x, J_y, J_z) = \sum_{\mu=1}^N (\sigma_x^\mu, \sigma_y^\mu, \sigma_z^\mu)$, with $\mu = 1, \dots, N$ identical particles, and the following identifications are made $J_+ = S_{10}, J_- = S_{01}, J_z = \frac{1}{2}(S_{11} - S_{00})$. In addition, if the total number of particles is conserved, there is

an extra conserved quantity: $C_1 = S_{00} + S_{11}$ (the linear Casimir operator of $U(2)$).

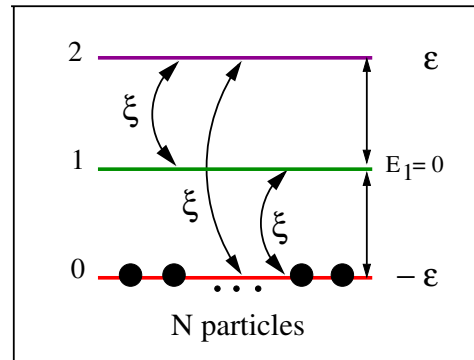


FIG. 1: Schematic image of the 3-level Lipkin model used in this work, described by Hamiltonian (4).

In this work, the 3-level LMG Hamiltonian with a fixed number of particles is considered

$$H = \sum_{i=0}^2 E_i S_{ii} - \sum_{i \neq j=0}^2 \xi_{ij} S_{ij}^2, \quad (3)$$

where E_i is the energy of the i -level and ξ_{ij} are the strengths of the two-body interaction between levels i and j . In this work, we have considered the same strength $\xi = \xi_{ij}; \forall i, j$ (control parameter) in all levels for the two-body interaction scattering pairs of particles and equal energy spacing, ε , between levels, as in previous studies [17, 18, 31–35]. We have taken $E_1 = 0$ as represented in Fig. 1. In addition, the total number of particles $N = S_{00} + S_{11} + S_{22}$ (the linear Casimir operator of $U(3)$) is conserved. In this situation, and using the $U(3)$ collective operators, the Hamiltonian takes the form,

$$H = \varepsilon(S_{22} - S_{00}) - \xi \sum_{i \neq j=0}^2 S_{ij}^2. \quad (4)$$

We can conveniently renormalize one-body interactions $\varepsilon \rightarrow \varepsilon/N$ by the total number N of particles, and two-body interactions $\xi \rightarrow \xi/[N(N-1)]$ by a factor related to the total number $N(N-1)/2$ of pairs. Furthermore, we reduce the total number of parameters by expressing the Hamiltonian dimensionless, that is dividing both terms in (4) by ε and setting $\xi/\varepsilon \rightarrow \lambda$. In addition to all these simplifications, it is convenient to multiply the one-body interactions by $(1-\lambda)$ in order to achieve a compact form of the Hamiltonian $H = (1-\lambda)H_0 - \lambda H_1$, with a bounded control parameter $\lambda \in [0, 1]$. This reparametrization allows us to characterize chaotic regions of the eigenspectrum and ESQPT for finite values of $\lambda \simeq 1$ (see Sec. IV B), preventing the selection of high values of λ as in [17, 35]. In summary, the Hamiltonian density used in this work is written as

$$H = \frac{(1-\lambda)}{N} (S_{22} - S_{00}) - \frac{\lambda}{N(N-1)} \sum_{i \neq j=0}^2 S_{ij}^2. \quad (5)$$

As in the two-level case, the model exhibits parity symmetry. That is, the interaction only scatters pairs of particles, so that the population S_{kk} in each level $k = 0, 1, 2$ conserves the even (+) or odd (-) parity. The operators related to this conservation are $\Pi_k = \exp(i\pi S_{kk})$. Hence, four different Hamiltonian independent sectors are identified by (Π_0, Π_1, Π_2) ,

$$\begin{aligned} (+, +, +), (-, -, +), (-, +, -), (+, -, -) & \quad N \text{ even} \quad (6) \\ (-, -, -), (+, +, -), (+, -, +), (-, +, +) & \quad N \text{ odd} \end{aligned}$$

This discrete symmetry corresponds to the finite group $\mathbb{Z}_2 \times \mathbb{Z}_2 \times \mathbb{Z}_2$, with the constraint $\Pi_0 \Pi_1 \Pi_2 = e^{i\pi N}$. The parity symmetry is broken in the thermodynamic limit, so the ground state becomes highly degenerated for the case $D = 3$ compared to $D = 2$.

For the sake of simplicity, we consider indistinguishable particles and reduce the Hilbert space dimension from 3^N to $d = \binom{N+2}{2} = \frac{(N+1)(N+2)}{2}$, corresponding to the fully symmetric irreducible representation of $U(3)$ [36]. As a consequence, computational complexity is reduced for large N . The rest of the mixed permutation symmetry sectors have already been studied in [35]. In the fully symmetric case, the Hilbert space is spanned by the Bose-Einstein-Fock basis states

$$|\vec{n}\rangle = |n_0, n_1, n_2\rangle = \frac{(b_0^\dagger)^{n_0} (b_1^\dagger)^{n_1} (b_2^\dagger)^{n_2}}{\sqrt{n_0! n_1! n_2!}} |\vec{0}\rangle, \quad (7)$$

where $|\vec{0}\rangle$ is the Fock vacuum, and n_i is the occupancy number of level i (the eigenvalue of S_{ii}). The total number of particles is restricted by the expression $n_0 + n_1 + n_2 = N$. A general symmetric N -particle state ψ in the Fock basis is written as $|\psi\rangle = \sum c_{\vec{n}} |\vec{n}\rangle$ where the sum is restricted to $n_0 + n_1 + n_2 = N$. Hence the matrix elements of the collective $U(3)$ -spin operators (2) in the Fock basis are

$$\begin{aligned} \langle \vec{m} | S_{ii} | \vec{n} \rangle &= n_i \delta_{\vec{m}, \vec{n}}, \quad (8) \\ \langle \vec{m} | S_{ij} | \vec{n} \rangle &= \sqrt{(n_i + 1) n_j} \delta_{m_i, n_i + 1} \delta_{m_j, n_j - 1} \prod_{k \neq i \neq j} \delta_{m_k, n_k}. \end{aligned}$$

With these matrix elements, the construction of the Hamiltonian density (5) matrix and its diagonalization are easy and provide the complete energy spectrum for a given number of particles, N . In Figure 2, the exact numerical energy densities (energy per particle E/N) results are plotted against the control parameter, λ , for $N = 15$ particles, in the top panel, and for $N = 100$ particles, in the bottom panel. In the diagonalization, the four previously mentioned parity sectors are separated. In this figure, regions around the center of the plot present energy clusters that create an increase of the energy level density typical of an ESQPT. However, the complexity of the spectrum level crossings makes the classification and analysis of these regions difficult. A hint to make this analysis comes from the mean field study valid in the thermodynamic limit, $N \rightarrow \infty$. All the diagonalization data is available at the public repository [37].

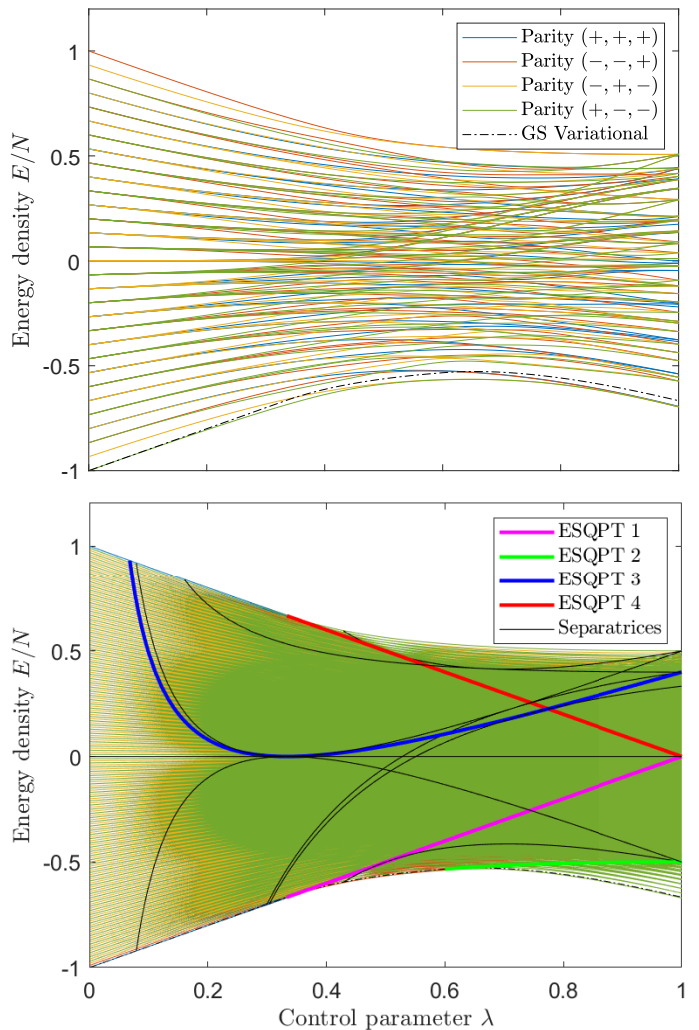


FIG. 2: Energy density (energy per particle E/N) of the symmetric representation of the 3-level LMG model as a function of the control parameter λ , for $N = 15$ (top) and $N = 100$ (bottom) particles. In both pictures, the thin lines represent the numerical energies, whose colors describe the parity sector in which they have been calculated. The dashed-dotted black line is the variational ground state (12), whose convergence to the numerical GS increases with N . The thick colored lines in the bottom spectrum represent the most relevant ESQPT separatrices (13), (14), while the rest are given in thin black lines (B2).

III. MEAN FIELD: ENERGY SURFACE AND PHASE DIAGRAM

Coherent states are used to reproduce the ground-state energy of Hamiltonian models in the limit $N \rightarrow \infty$, called the semiclassical or the thermodynamic limit. Therefore, they are often called semiclassical or variational states. $U(3)$ -spin coherent states (3SCSs for brevity) are defined

as

$$|\mathbf{z}\rangle = \frac{1}{\sqrt{N!}} \left(\frac{b_0^\dagger + z_1 b_1^\dagger + z_2 b_2^\dagger}{\sqrt{1 + |z_1|^2 + |z_2|^2}} \right)^N |\vec{0}\rangle, \quad (9)$$

where $z_1, z_2 \in \mathbb{C}$ are variational parameters, and the coherent state is associated with N particles in total. The Appendix A is devoted to studying 3SCSs in detail.

Using the 3SCS expectation value of the Hamiltonian density (5), and taking the thermodynamic limit, we define the energy surface as $E(\mathbf{z}, \lambda) = \lim_{N \rightarrow \infty} \langle \mathbf{z} | H | \mathbf{z} \rangle$. With the linear $\langle \mathbf{z} | S_{ij} | \mathbf{z} \rangle$ and quadratic $\langle \mathbf{z} | S_{ij} S_{kl} | \mathbf{z} \rangle$ matrix elements given in (A3), the explicit form for the energy surface is,

$$E(\mathbf{z}, \lambda) = (1 - \lambda) \frac{|z_2|^2 - 1}{1 + |z_1|^2 + |z_2|^2} - \lambda \frac{z_1^2 (\bar{z}_2^2 + 1) + z_2^2 + \text{c.c.}}{(1 + |z_1|^2 + |z_2|^2)^2}. \quad (10)$$

The parity symmetry $z_1 \rightarrow -z_1, z_2 \rightarrow -z_2$ is inherited from the Hamiltonian (5).

The ground-state energy corresponds to the variational minimum $E_0(\lambda) = \min_{z_1, z_2 \in \mathbb{C}} E(z_1, z_2, \lambda)$, which is attained at the critical (real) coherent state parameters

$$z_{1\pm}^{(0)}(\lambda) = \pm \begin{cases} 0, & 0 \leq \lambda \leq \frac{1}{3}, \\ \sqrt{\frac{3\lambda-1}{\lambda+1}}, & \frac{1}{3} \leq \lambda \leq \frac{3}{5}, \\ \sqrt{\frac{2\lambda}{-\lambda+3}}, & \lambda \geq \frac{3}{5}, \end{cases} \quad (11)$$

$$z_{2\pm}^{(0)}(\lambda) = \pm \begin{cases} 0, & 0 \leq \lambda \leq \frac{3}{5}, \\ \sqrt{\frac{5\lambda-3}{-\lambda+3}}, & \lambda \geq \frac{3}{5}. \end{cases}$$

Inserting (11) into (10) gives the ground-state energy density in the thermodynamic limit

$$E_0(\lambda) = \begin{cases} -1 + \lambda, & 0 \leq \lambda \leq \frac{1}{3}, & \text{(I)} \\ -\frac{(1+\lambda)^2}{8\lambda}, & \frac{1}{3} \leq \lambda \leq \frac{3}{5}, & \text{(II)} \\ 1 - \frac{1}{2\lambda} - \frac{7\lambda}{6}, & \lambda \geq \frac{3}{5}. & \text{(III)} \end{cases} \quad (12)$$

This energy is plotted in Figure 2 with a dashed-dotted line under the name GS-variational. As we already anticipated, the ground state is degenerated, since there are four different 3SCSs $|z_{1\pm}^{(0)}, z_{2\pm}^{(0)}\rangle$ with the same energy (12) in the thermodynamic limit $N \rightarrow \infty$. For real systems, there are finite size effects that slightly modify the ground state, but in Figure 2 is observed that the exact numerical calculation follows closely the mean field result. Naturally, the larger N is, the better the agreement (see the bottom panel). According to the mean field calculation for the ground-state energy, there are three different phases (I, II and III) separated by two second-order QPTs (according to Ehrenfest's classification) occurring at critical points $\lambda_{\text{I} \leftrightarrow \text{II}}^{(0)} = 1/3$ and $\lambda_{\text{II} \leftrightarrow \text{III}}^{(0)} = 3/5$, respectively, at which the second derivative of $E_0(\lambda)$ is discontinuous.

In the numerical calculation, the complete energy spectrum is obtained, Figure 2, and the mean field calculation might help to understand the different structures observed in the excitation spectrum. These are related to the stationary points that appear in the energy surface formula (10). These are usually called ESQPT separatrices and can be computed as the solutions of the equation $\nabla_{\mathbf{z}} E(\mathbf{z}, \lambda) = \mathbf{0}$ [6, 38]. Inserting the stationary points into the energy surface formula (10), we obtain 14 separatrices that are given explicitly in Appendix B and are plotted in Figure 2 (bottom panel) as black lines. Some of them are especially important to study ESQPTs. The first of them is defined by the extension of the GS state energies (12) of phase I and II to larger values of the control parameter, that is

$$f_1(\lambda) = -1 + \lambda, \quad \forall \lambda \geq \frac{1}{3}, \quad \text{(ESQPT1, magenta)}$$

$$f_2(\lambda) = -\frac{(1+\lambda)^2}{8\lambda}, \quad \forall \lambda \geq \frac{3}{5}. \quad \text{(ESQPT2, green)} \quad (13)$$

These are graphically presented by the thick magenta and green lines in Figure 2 in the bottom panel for $N = 100$ particles. Some other representative separatrices (B2), selected as they provide a classification rule for the different chaotic regions (see Eq.(18)) as we will see in the next sections, are

$$f_3(\lambda) = \frac{(1-3\lambda)^2}{10\lambda}, \quad \forall \lambda \geq \frac{1}{19}(8 - 3\sqrt{5}), \quad \text{(ESQPT3, blue)}$$

$$f_4(\lambda) = 1 - \lambda, \quad \forall \lambda \geq \frac{1}{3}. \quad \text{(ESQPT4, red)} \quad (14)$$

The ESQPT separatrices of Eqs.(13) and (14) are marked with representative colors (magenta, green, blue and red in order) along the figures of this manuscript.

In order to investigate and clarify the role of these ESQPT separatrices, the density of states (DOS) is computed from the energy spectrum of Figure 2 bottom panel, for selected fixed λ values. The calculated DOS are depicted in Figure 3. To construct this figure, we use 100 bin histograms and some representative values of the control parameter $\lambda = 0.2, 0.4, 0.65$, and 0.98 in the three different QPT regions (12), trying to avoid zones with an agglomeration of separatrices that can obscure the discussion. In Figure 3, the colored vertical dashed lines are separatrices (13) and (14) marking changes in the shape and curvature of the DOS, often associated to ESQPT [6]. This is better represented in the smoothed DOS, which is the solid black line in the plot. We have used a Gaussian-weighted moving average (MA) filter to smooth the DOS, with a window size of 15 elements. This procedure will be detailed in the coming Section IV B. The deformation of the DOS when the control parameter is increased evinces how the interaction destroys the symmetry of the Hamiltonian, H (5). To better understand the role of the separatrices (13) and (14), we study the chaoticity of the energy spectrum in the next section.

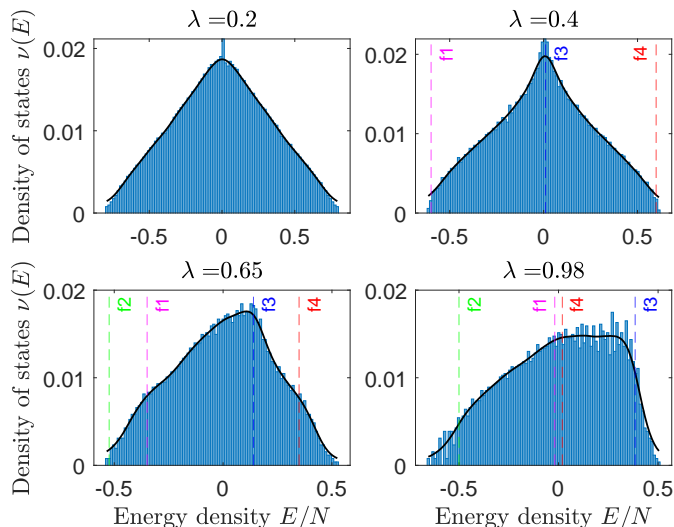


FIG. 3: Histogram of 100 bins representing the density of states of the 3-level LMG model for $N = 100$ particles and for some representative values of the control parameter λ in the three QPT regions. The solid black line is the smoothed DOS with a MA window size of 15 elements. The dashed vertical lines represent the ESQPT separatrices (13), and (14).

IV. RESULTS

A. Poincaré sections and Peres lattices

If a quantum system is regular or non-chaotic, then its classical analog system is integrable. Therefore, to study the regularity of the 3-level LMG Hamiltonian, one should examine the dynamics of the model in its classical limit. We can arrive at the classical LMG Hamiltonian in terms of its canonical momentum and position variables, p and q respectively, by making use of the following changes of variables:

$$\beta_j \equiv \frac{z_j}{(1 + |z_1|^2 + |z_2|^2)^{1/2}}, \quad j = 1, 2, \quad (15)$$

and then

$$\beta_j = \frac{q_j + ip_j}{\sqrt{2}}. \quad (16)$$

Applying these to Eq. (10), we arrive at

$$\begin{aligned} E(q, p, \lambda) = & -(1 - \lambda) + \frac{1}{2}q_1^2(1 - 3\lambda) \\ & + \frac{1}{2}q_2^2(2 - 3\lambda) + \frac{1}{2}p_1^2(1 + \lambda) + p_2^2 \\ & + \frac{1}{2}\lambda((q_1^2 + q_2^2)^2 - (p_1^2 + p_2^2)^2) \\ & - (q_1^2 - p_1^2)(q_2^2 - p_2^2) - 4q_1q_2p_1p_2. \end{aligned} \quad (17)$$

Now, if a system with two degrees of freedom is integrable, then there is a second conserved quantity in addition to the energy, which forces the trajectories to

lie on a two-dimensional torus in the phase space. If we take a Poincaré surface section of these trajectories, in this case, the intersection of the trajectories with a plane of a particular λ and energy value, these tori manifest as closed curves within the plane. Meanwhile, if the system is chaotic, the Poincaré section consists of a set of points evenly covering the available phase space without any particular structure. For any case that lies in between, the sections will have chaotic regions of evenly distributed points as well as closed curves.

In Figure 4 we represent the (q_2, p_2) Poincaré sections of the classical Hamiltonian in Eq.(17) at $\lambda = 0.98$. The sections cut the plane $q_1 = q_{10}$, where the equilibrium value $q_{10}^2 = 2/3$ is obtained from the potential energy surface $E(q, p = 0, \lambda)$ minimization. Furthermore, the conservation of the total number of particles $q_1^2 + q_2^2 + p_1^2 + p_2^2 \leq 2$ and $\dot{q}_1 \geq 0$ are necessary constraints for the Poincaré section calculation.

The energies chosen in Figure 4 lie in the regions between the ESQPTs defined in Eqs. (13), (14) and correspond to chaotic (top right panel), quasi-chaotic (bottom left) and quasi-integrable (diagonal panels) regions. That is, we propose an analytical model for $\lambda \simeq 1$ which demarcates the dynamical classes using ESQPT separatrices, highlighting the connection between chaos and ESQPT [13, 39–42],

$$\begin{aligned} \text{Quasi-int.} & \quad E \leq -\frac{(1+\lambda)^2}{8\lambda} & (E_0 \text{ to } f_2), \\ \text{Chaotic} & \quad E \in \left(-\frac{(1+\lambda)^2}{8\lambda}, -1 + \lambda\right] & (f_2 \text{ to } f_1), \\ \text{Quasicha.} & \quad E \in \left(-1 + \lambda, \frac{(1-3\lambda)^2}{10\lambda}\right] & (f_1 \text{ to } f_3), \\ \text{Quasi-int.} & \quad E > \frac{(1-3\lambda)^2}{10\lambda} & (f_3 \text{ to } E_{\max}). \end{aligned} \quad (18)$$

This classification for $\lambda \simeq 1$ is shown in the bottom panel of Figure 2, where different groups of separatrices merge with the colored ones in $\lambda \rightarrow 1$, simplifying the spectrum classification in dynamical regions. The sections showcase the complexity of the spectrum and the challenge of ESQPT characterization, with multiple regions of varying regularity and chaos. It is important to note the necessity of selecting a value of the control parameter $\lambda = 0.98 \simeq 1$, where we have a reasonable energy range with completely integrable and chaotic dynamics separately. We include a collection of animations of the Poincaré section plots for different values of λ and the energy in the supplemental material [43], where the lack of a wide energy range of integrable states can be observed. This limitation in λ is also required in Figures 6, 7, 9, and 10 to display regions with a reasonable chaotic or quasi-integrable character. In fact, the selected $\lambda = 0.98$ coincides with the control parameters $\chi = 100$ chosen in the bibliography [15–18], where the reparameterization $\lambda = \frac{\chi/2}{1-\chi/2}$ is necessary to map the Hamiltonian (4) to our model (5). We also mention that the role of the separatrix f_4 (14) in the classification (18) is neglected as $f_1(\lambda) \simeq f_4(\lambda)$ for the case of study $\lambda = 0.98$.

In addition to the Poincaré sections, we also study some of the so-called Peres lattices of the system. When the classical analog $E(q, p, \lambda)$ is integrable, the Einstein–Brillouin–Keller (EBK) quantization becomes a good approximation in the semiclassical limit, making it so that the energy spectra is regularly distributed. This can easily be seen in Fig. 2 for $\lambda = 0$, where the system is integrable, and the energies are equally spaced, but becomes unclear as λ increases, and the system presents more chaotic regions. Nevertheless, this regularity property holds for the eigenvalues of any conserved dynamical variable, not only the Hamiltonian, and therefore, by plotting the expected values of these conserved quantities vs the energy spectra, the chaos of the system can be studied. If the system is integrable, then the EBK approximation holds and both observables will be distributed in a regular lattice when plotted against each other, while failure to do so is indicative of quantum chaos [21].

Here we consider the expected values of the collective spin operators S_{ii} . In particular, Fig. 5 shows the Peres lattices of $|\langle S_{11} \rangle / N|$ vs the energy density of the Hamiltonian. Additionally, ESQPT 1, 2, 3, and 4 separatrices (13), and (14) are also represented. We have already seen from the energy spectra that the system is integrable for $\lambda = 0$ and that, at higher values of λ , chaotic and quasi-chaotic regions start to appear, but notably, Fig. 5 shows that quasi-chaotic regions already appear at small values of λ , which was not clearly seen through the density of states. The results for other S_{ii} operators show similar trends.

Finally, the chosen separatrices can be used to delimit the different regions at high values of λ as we move up from the ground state to higher excited states, being quasi-integrable up to ESQPT2, then chaotic from ESQPT2 to ESPQT1, quasi-chaotic from ESPQT4 to ESPQT3, and again quasi-integrable after ESQPT3. As expected, for middle values of λ , delimiting these regions is much harder as the spectrum is more complex, ESQPTs cross each other, and the regions overlap. Nevertheless, one can still qualitatively identify some chaotic, quasi-chaotic, or quasi-integrable regions from the distribution of points in the Peres lattices.

B. Unfolded spectrum and nearest-neighbors spacing distribution

We perform an unfolding procedure to smooth the DOS and extract a local average function of it [44]. It allows us to erase spectral fluctuations and compare spectra in an unbiased manner [17]. Firstly, we compute a histogram of the DOS $\rho(E)$ (using numerical diagonalization data) and smooth it $\rho_\Delta(E)$ with a Gaussian filter of variance Δ^2 . In practice, we set the window size of a Gaussian-weighted moving average (MA) filter in place of Δ^2 . Then we calculate the cumulative distribution function of the numerical data $\sigma(E)$ (level staircase), and the

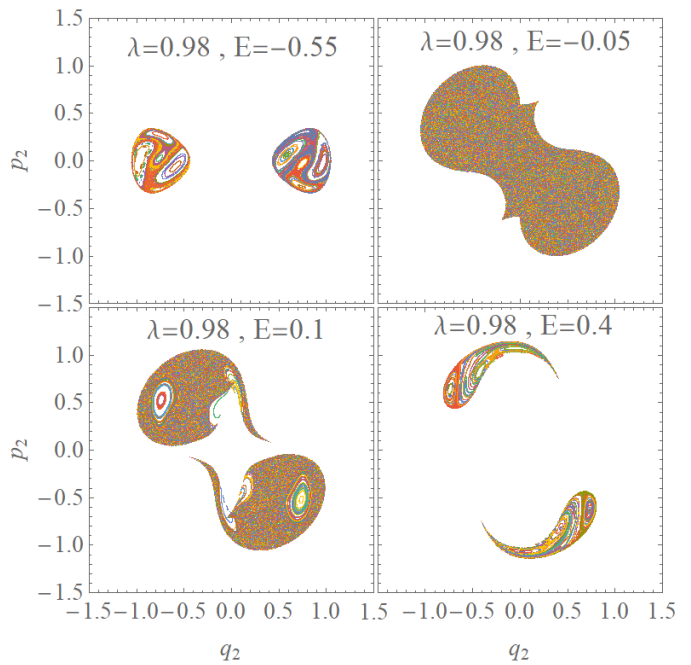


FIG. 4: Poincaré sections of the energy surface in the position and momentum space (17), for a fixed value of the control parameter $\lambda = 0.98$ and some representative values of the energy E inside each dynamical region (18). The sections are plotted in the (q_2, p_2) space for crossings with the $q_1 = 0.8165$ plane, the equilibrium value of q_1 . Quasi-integrable trajectories are depicted in the diagonal subplots of the grid. Quasichaotic and chaotic trajectories are shown in the bottom left and top right subplots respectively.

integral of the smoothed DOS $\sigma_\Delta(E)$ (trapezoidal numerical integration). After that, we compare both distributions $\sigma(E)$ and $\sigma_\Delta(E)$ using a two-sample Kolmogorov-Smirnov test [45], and choosing the optimal window size that minimizes the test error. Eventually, we fit the values of $\sigma_\Delta(E)$ with a cubic spline to obtain a function defined in a continuous domain $E \in \mathbb{R}$, and identify the unfolded spectrum as $e_i = d \cdot \sigma_\Delta(E_i)$, with d the Hilbert space dimension and E_i the numerical energies.

We use a MA window size of 15 elements and $N = 100$ to calculate the smoothed DOS $\rho_\Delta(E)$, over a histogram of 200 bins for the DOS $\rho(E)$. Then, we perform the Kolmogorov-Smirnov test that gives a statistic equal to 0.015 and a p -value equal to 1, so we fail to reject the null hypothesis that the two samples $\sigma(E)$ and $\sigma_\Delta(E)$ are from the same continuous distribution at the 5% significance level.

Using the normalized energy spacings $s_i = (e_{i+1} - e_i) / \bar{e}$ of the unfolded spectrum, we can define the nearest-neighbor spacing distribution (NNSD) as the probability $P(s)$ that two neighboring eigenvalues are a distance s apart. The energy levels are classified into the dynamical classes defined in equation (18): chaotic, qua-

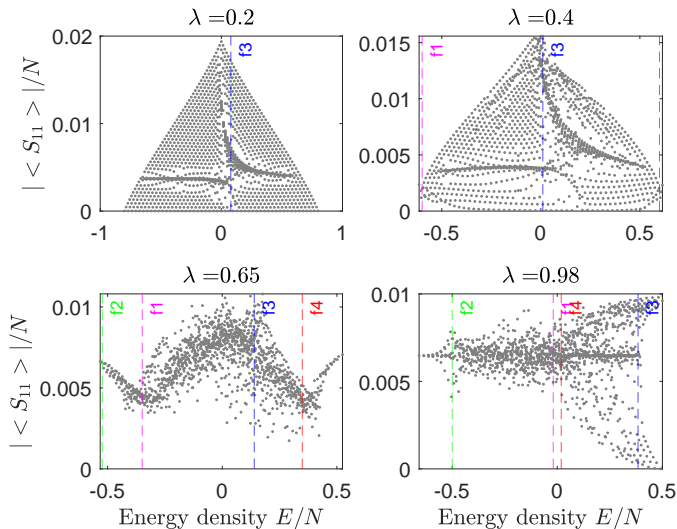


FIG. 5: Peres lattices for the expected values $|\langle S_{11} \rangle|/N$ vs the different excitation energies of the 3-level LMG model. We choose $N = 100$ particles, some representative values of the control parameter λ in each column, and we restrict to the parity sector $p = (+, +, +)$ for the sake of clarity. The dashed vertical lines represent the ESQPT separatrices (13), (14). Similar results are obtained for $\langle S_{22} \rangle$, $\langle S_{00} \rangle$ and $\langle S_{22} - S_{00} \rangle$.

sichaotic, and quasi-integrable. The chaotic ones will have a NNSD with Wigner distribution shape $P_W(s) = \frac{\pi}{2} s \exp(-\frac{\pi}{4} s^2)$, and the quasi-integrable ones a Poisson distribution shape $P_P(s) = \exp(-s)$. This is presented in Figure 6 for $N = 100$ and $\lambda = 0.98$, where the three dynamical classes are shown in each subplot, and the solid and dashed-dotted lines represent the Wigner and Poisson distributions respectively. The pictures also present a qualitative measure of the degree of chaos, the parameter η , which is introduced in the coming paragraph (19). To obtain a better fit of the histograms to the distributions, we use 200 bins in the DOS and a MA window of 15 elements when smoothing. In addition, the level classification (18), the unfolded spectrum and the energy spacings are conveniently computed in each parity sector of the Hamiltonian, and then the results are merged to calculate the NNSD histogram of Figure 6. The bottom panel represents the states in quasi-integrable regions (E_0, f_2) and (f_3, E_{\max}), the top panel in the chaotic (f_2, f_1), and the middle panel in the quasichaotic (f_1, f_3).

In order to quantitatively delimit the energy range of each class, we measure the degree of chaos with the following expression [46]

$$\eta = \frac{\sigma_s - \sigma_W}{\sigma_P - \sigma_W}, \quad (19)$$

with $\sigma_W = 4/\pi - 1$ and $\sigma_P = 1$ the variance of the Wigner and Poisson distribution respectively, and σ_s the variance of the NNSD in question. More explicitly, we

select several consecutive spacings s (200 for example, without considering the dynamical regions (18)), compute the NNSD and its associated value of η (19), and repeat the process for a new sequence of spacings. The values η are plotted versus the mean energy of each sequence in Figure 7, for the parity $p = (+, +, +)$, $N = 100$ particles and $\lambda = 0.98$. While the analysis of individual parity sectors yields similar results, the superposition of all parity sectors obscures the characterization of the system's chaoticity. In this figure, we compute the unfolded spectrum for a DOS histogram with 200 bins, a MA window of 15 elements, and to calculate η we select sequences of 70 energy spacings. High values of η appear to the left and right of the separatrices f_1 (green) and f_3 (blue) respectively, corresponding to the integrable regime (Poisson distribution $\sigma_P = 1$). In contrast, the degree of chaos has reduced values for the energies between these two separatrices, which is characteristic of a chaotic regime (Wigner distribution $\sigma_W \simeq 0.27$).

We also include a second measure of chaoticity, called the Kullback–Leibler (KL) divergence [23]

$$D_{\text{KL}}(P||Q) = \sum_s P(s) \log\left(\frac{P(s)}{Q(s)}\right), \quad (20)$$

where $P(s)$ is the NNSD and $Q(s) = P_W(s)$ is the Wigner distribution. The KL divergence compares the NNSD with a Wigner distribution; that is, it gives a value of 0 for chaotic distributions and values greater than zero otherwise. In Figure 8, the KL divergence is plotted for the same parameters as those used in the degree of chaos Figure 7, but using all parity sectors at once. We observe a drop in the KL divergence when crossing the first separatrix f_2 (green), delimiting quasi-integrable and chaotic regimes. Then, after the separatrices f_1 and f_4 (red), the divergence starts growing again in the quasichaotic regime, and stabilizes after the separatrix f_3 (blue) in the second quasi-integrable regime zone. The KL divergence gives better qualitative evidence of chaoticity and ESQPT than the degree of chaos.

C. Participation ratio and susceptibility

We also characterize the ESQPT with the Participation Ratio (PR), which is defined as

$$PR(\lambda, E_j) = \frac{1}{\sum_{\|\vec{n}\|_1=N} |c_{\vec{n},j}(\lambda)|^4},$$

with $c_{\vec{n},j}$ the components of the eigenstates $|\psi_j(\lambda)\rangle$ expressed in the Fock basis, with energies E_j . It is plotted for $N = 100$ and $\lambda = 0.98$ in Figure 9, where we perform a MA smoothing with 15 elements window to damp the strong oscillations of the PR. Following the classification in (18), there is a PR cluster to the left of f_2 corresponding to the quasi-integrable states. The PR points spread to the right of this separatrix, introducing the chaotic region. The line f_1 is close to a local minimum in the

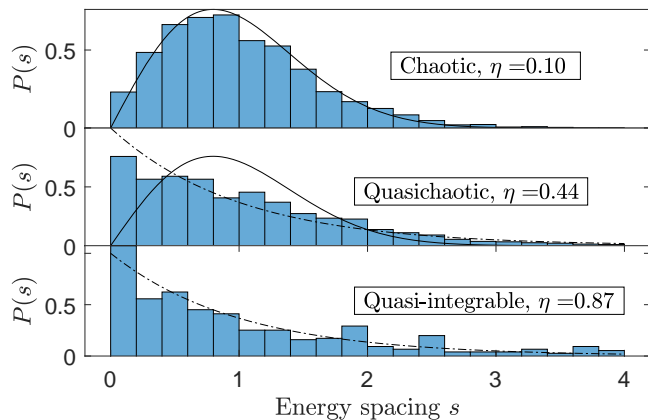


FIG. 6: Nearest-neighbors spacing distribution of the 3-level LMG model for $N = 100$ particles, and $\lambda = 0.98$. The unfolded spectrum is computed over a DOS histogram of 200 bins, smoothed by a Gaussian filter with a moving average window of 15 elements [44]. The energies included in the NNSD calculation of each subplot are delimited by the regions defined in (18). That is, the bottom panel represents the states in quasi-integrable regions (E_0, f_2) and (f_3, E_{\max}) , the top panel in the chaotic (f_2, f_1) region, and the middle panel in the quasichaotic (f_1, f_3) region. We also display the η degree of chaos (19) on top, and plot the Wigner (solid) and Poisson (dashed-dot) distributions.

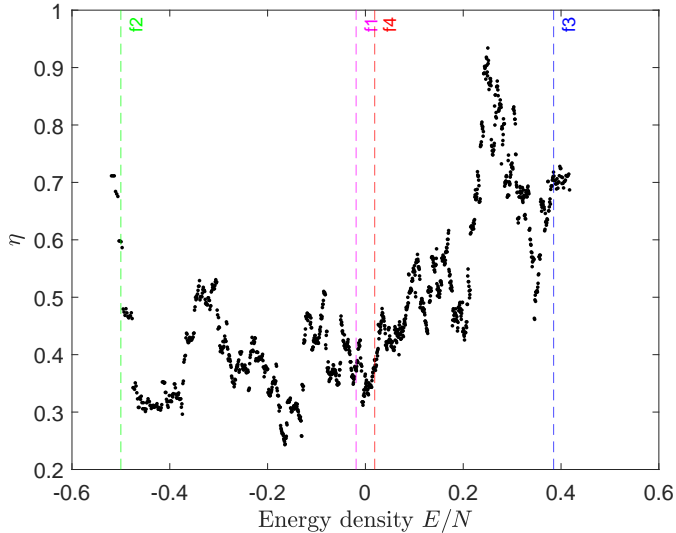


FIG. 7: Degree of chaos η (19) of the 3-level LMG model for $N = 100$ particles, $\lambda = 0.98$, and parity $p = (+, +, +)$. To compute each value of η , we select sequences of 70 energy spacings and calculate the corresponding NNSD. Previously, the spectrum is unfolded over a DOS histogram of 200 bins, smoothed by a Gaussian filter with a 15 elements window [44]. The dashed vertical lines represent the ESQPT separatrices (13), and (14).

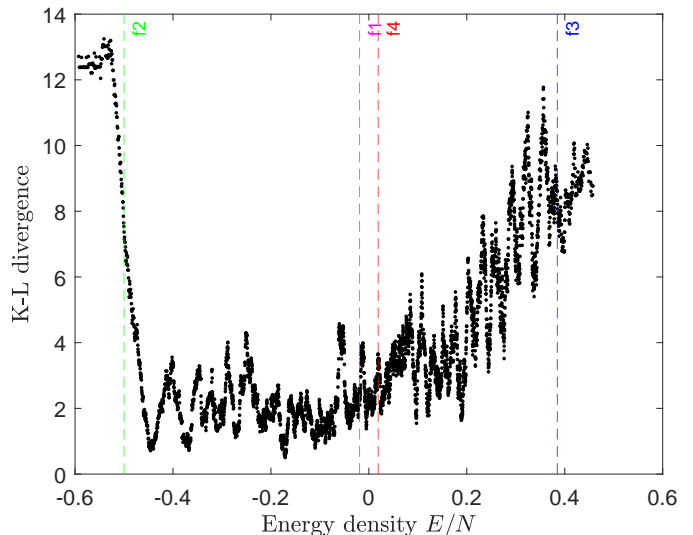


FIG. 8: Kullback–Leibler divergence of the 3-level LMG model for $N = 100$ particles and $\lambda = 0.98$. To compute each value of D_{KL} , we select sequences of 70 energy spacings and calculate the corresponding NNSD (20 bins histogram with $s_{\max} = 4$). Previously, the spectrum was unfolded over a DOS histogram of 200 bins, smoothed by a Gaussian filter with a 15 elements window [44]. The dashed vertical lines represent the ESQPT separatrices (13), and (14).

top points with higher PR, characterizing the ESQPT1 and the beginning of the quasichaotic region. The last line f_3 identifies a local drop of the PR corresponding to the ESQPT3 and the start of the second quasi-integrable region.

D. Overlap distribution

The overlap distribution is computed as the scalar product of an eigenstate of the LMG Hamiltonian $|\psi_j(\lambda)\rangle$ [17], $j = 1, \dots, d$, and the basis states $|\vec{n}\rangle$ of the Hilbert space (7). The overlap $x_{j,\vec{n}}(\lambda) = \langle \psi_j(\lambda) | \vec{n} \rangle$ is computed for a fixed value of the control parameter λ and for all the combinations of the indexes j and \vec{n} , giving a total of d^2 values, whose frequencies are represented with a normalized distribution in the histogram of Figure 10. With the yellow color, we represent states in the quasi-integrable regime for $N = 100$, $\lambda = 0.98$ and parity $p = (+, +, +)$, which have a delta-like distribution since an integrable system is expressed in terms of only a few states of the basis. In blue and red, chaotic and quasichaotic states resemble a Gaussian shape, which is characteristic of the states in a Gaussian Orthogonal Ensemble (GOE), so the overlap $x_{j,\vec{n}}$ can be seen as a Gaussian random variable in this case [44, 47]. Similar results are obtained for the rest of the parities (6).

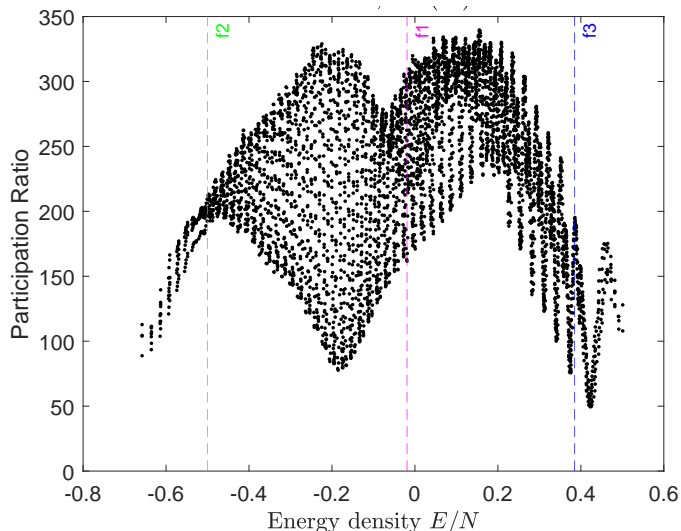


FIG. 9: Participation ratio of the 3-level LMG model for $N = 100$ and $\lambda = 0.98$. Each dot represents the PR of a numerical eigenstate with energy E . The plot is smoothed with a MA of 15 elements window. The dashed vertical lines represent the ESQPT separatrices (13), and (14).

V. CONCLUSIONS

We have characterized the ESQPT of the 3-level LMG using a wide range of indicators. Starting from the numerical calculations, the energy surface for a low number of particles $N = 15$ presents clusters of levels, forecasting where the ESQPT will be found. When the dimensionality increases to $N = 100$ particles, the energy spectrum becomes complex and the ESQPT cannot be visually characterized. Hence, we make use of the mean field limit to find the ESQPT separatrices. The energy surface minimization results in a long list of stationary points with degeneration, which can be reduced to 14 different separatrices. At this point, a connection between chaos and ESQPT is made, using four of these separatrices to define the following dynamical classes: quasi-integrable, chaotic, and quasichaotic. The classification can only be made for high values of the interaction $\lambda \simeq 1$, due to the lack of a wide energy range of integrable states for the rest of λ values. The dynamical regions are graphically represented by Poincaré sections and Peres lattices for $N \rightarrow \infty$ and $N = 100$ respectively. Regular patterns are observed in the quasi-integrable regions, whereas scattered points appear in the chaotic ones.

The numerical spectrum is also depicted with the density of states histogram, where the changes in curvature are associated with the four main ESQPT separatrices. To erase spectral fluctuations, the unfolding procedure smooths the DOS, so we can compute the nearest-neighbor spacing distribution. For high interaction $\lambda = 0.98$, the spacing distributions resemble the Wigner and Poisson shapes in the chaotic and quasi-

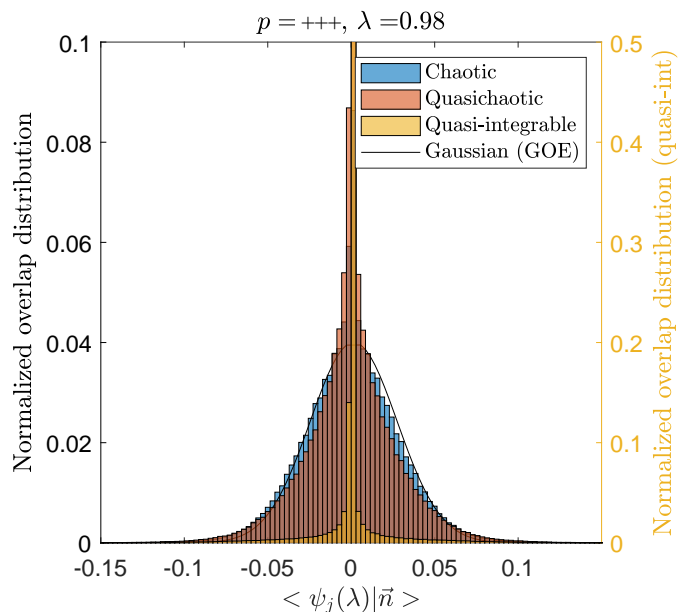


FIG. 10: Normalized overlap distribution $\langle \psi_j(\lambda) | \vec{n} \rangle$ of the 3-level LMG model for $N = 100$, $\lambda = 0.98$ and the parity sector $p = (+, +, +)$. The different colors represent the dynamical regions in (18), with the left y-axis referring to chaotic and quasichaotic regimes, and right y-axis to quasi-integrable. Similar results are obtained for the other parity sectors (6).

integrable regions respectively, demonstrating the utility of computing ESQPT separatrices analytically to detect chaos numerically afterwards. In addition, we provide two magnitudes that measure the chaoticity of the spacing distribution, the degree of chaos η and the Kullback–Leibler divergence. Both present low and high values for chaotic and quasi-integrable classes respectively, with the KL divergence having the best performance and matching of the separatrices. Finally, the participation ratio and the overlap distribution are presented to detect ESQPTs and dynamical classes respectively.

In general, the characterization of ESQPT and chaos is consistent for high values of the interaction parameter λ , but limited elsewhere due to two main causes: the variety of stationary points of the mean field energy surface (B2) (that merge at $\lambda \simeq 1$, see Fig.2), and the impossibility to distinguish quasi-integrable and chaotic regions [43]. For this reason, we would like to extend the ESQPT analysis in further works to other permutation symmetry sectors of the 3-level LMG model [35, 48], and also to the 3-level extension of other models such as the Jaynes-Cummings [49, 50], Dicke [51, 52] or Agassi [53, 54] models.

The analytical and numerical techniques developed in this work establish a systematic method applicable to other models. In fact, the study of 3-level system spectra and dynamics has a direct impact on current research topics. The applications range from novel quantum sensing devices, such as NV-centers [55, 56], to the usage

of qutrits in quantum computation [57, 58]. The traditional 2-level (qubits) framework is transforming via the extension to more general and flexible level structures, which could eventually outperform the current quantum technologies [59, 60].

ACKNOWLEDGMENTS

This work is part of the I+D+i projects PID2022-136228NB-C22, and PID2023-146401NB-I00 funded by MICIU/AEI/10.13039/501100011033 and by ERDF, EU, and of the PPIT – FEDER project SOL2024-31833 at University of Sevilla. It has also been partially supported by the Consejería de Conocimiento, Investigación y Universidad, Junta de Andalucía (Spain) and European Regional Development Fund (ERDF) under the grant Group FQM-160. AM thanks the support of the Spanish Ministry of Science through the project PID2022-138144NB-I00. AS acknowledges that this work has been financially supported by the Ministry for Digital Transformation and of Civil Service of the Spanish Government through the QUANTUM ENIA project call - Quantum Spain project, and by the European Union through the Recovery, Transformation and Resilience Plan - NextGenerationEU within the framework of the Digital Spain 2026 Agenda.

Appendix A: U(3)-spin coherent states

The standard U(2)-spin coherent states are defined as a two-mode binomial expression [61–63]. U(3)-spin coherent states (3SCSs for brevity) are defined as a three-mode multinomial generalization (9). They are labeled by 2 complex numbers $\mathbf{z} = (z_1, z_2)^t \in \mathbb{C}^2$. In fact, we select certain patch of the complex projective manifold $\mathbb{C}P^2$, which is equivalent to choose $i = 0$ as reference level [64]. The total number of particles N is also a parameter of the 3SCS, omitted to simplify the notation.

The coefficients $c_{\bar{n}}(\mathbf{z})$ of the expansion of $|\psi\rangle = |\mathbf{z}\rangle$ in the Fock basis are simply

$$c_{\bar{n}}(\mathbf{z}) = \sqrt{\frac{N!}{\prod_{i=0}^2 n_i!}} \frac{\prod_{i=1}^2 z_i^{n_i}}{(1 + \mathbf{z}^\dagger \mathbf{z})^{N/2}}, \quad (\text{A1})$$

where $\mathbf{z}^\dagger \mathbf{z} = |z_1|^2 + |z_2|^2$ denotes the standard scalar product in \mathbb{C}^2 .

In general, 3SCSs are not orthogonal since the scalar product

$$\langle \mathbf{z} | \mathbf{z}' \rangle = \frac{(1 + \mathbf{z}^\dagger \mathbf{z}')^N}{(1 + \mathbf{z}^\dagger \mathbf{z})^{N/2} (1 + \mathbf{z}'^\dagger \mathbf{z}')^{N/2}} \quad (\text{A2})$$

is not necessarily zero. However, they are an overcomplete set of states closing a resolution of the identity [35, 64, 65].

3SCS matrix elements of 3-spin operators S_{ij} are easily computed from (8) and (A1),

$$\langle \mathbf{z}' | S_{ij} | \mathbf{z} \rangle = N \bar{z}'_i z_j \frac{(1 + \mathbf{z}'^\dagger \mathbf{z})^{N-1}}{(1 + \mathbf{z}'^\dagger \mathbf{z}')^{N/2} (1 + \mathbf{z}^\dagger \mathbf{z})^{N/2}}, \quad (\text{A3})$$

where we understand $z_0 = 1 = z'_0$. From here, 3SCS matrix elements of quadratic powers of 3-spin operators can be concisely written as

$$\langle \mathbf{z}' | S_{ij} S_{kl} | \mathbf{z} \rangle = \delta_{jk} \langle \mathbf{z}' | S_{il} | \mathbf{z} \rangle + \frac{N-1}{N} \frac{\langle \mathbf{z}' | S_{ij} | \mathbf{z} \rangle \langle \mathbf{z}' | S_{kl} | \mathbf{z} \rangle}{\langle \mathbf{z}' | \mathbf{z} \rangle}. \quad (\text{A4})$$

Note that

$$\lim_{N \rightarrow \infty} \frac{\langle \mathbf{z} | S_{ij} S_{kl} | \mathbf{z} \rangle}{\langle \mathbf{z} | S_{ij} | \mathbf{z} \rangle \langle \mathbf{z} | S_{kl} | \mathbf{z} \rangle} = 1, \quad (\text{A5})$$

which means that quantum fluctuations are negligible in the thermodynamic limit $N \rightarrow \infty$. These ingredients are compulsory when computing the energy surface in Section III.

Appendix B: Energy surface minimization: stationary points and ESQPT separatrices.

The global minimization of the energy surface (10), $E^{(0)}(\lambda) = \min_{z_1, z_2 \in \mathbb{C}} E(z_1, z_2, \lambda)$, is achieved at the critical (real) coherent state parameters

$$z_{1\pm}^{(0)}(\lambda) = \pm \begin{cases} 0, & 0 \leq \lambda \leq \frac{1}{3}, \\ \sqrt{\frac{3\lambda-1}{\lambda+1}}, & \frac{1}{3} \leq \lambda \leq \frac{3}{5}, \\ \sqrt{\frac{2\lambda}{-\lambda+3}}, & \lambda \geq \frac{3}{5}, \end{cases} \quad z_{2\pm}^{(0)}(\lambda) = \pm \begin{cases} 0, & 0 \leq \lambda \leq \frac{3}{5}, \\ \sqrt{\frac{5\lambda-3}{-\lambda+3}}, & \lambda \geq \frac{3}{5}. \end{cases} \quad (\text{B1})$$

Inserting (B1) into (10) gives the ground-state energy density (12) in the thermodynamic limit. The rest of the solutions of the equation $\nabla_{\mathbf{z}} E(\mathbf{z}, \lambda) = \mathbf{0}$, define the stationary points $\mathbf{z}^{(j)}$ of the LMG Hamiltonian. They establish a formalism to identify and classify the ESQPTs of quantum systems in the classical limit [6, 38]. The potential ESQPT separatrices are defined as energy surface evaluated in the stationary points $f_j(\lambda) = E(\mathbf{z}^{(j)}, \lambda)$,

whose expressions are listed below

$$\begin{aligned}
f_1(\lambda) &= -1 + \lambda, & \forall \lambda \geq 0, & \quad (\text{ESQPT1}) \\
f_2(\lambda) &= -\frac{(1+\lambda)^2}{8\lambda}, & \forall \lambda \geq \frac{1}{3}, & \quad (\text{ESQPT2}) \\
f_3(\lambda) &= \frac{(1-3\lambda)^2}{10\lambda}, & \forall \lambda \geq \frac{1}{19}(8 - 3\sqrt{5}), & \quad (\text{ESQPT3}) \\
f_4(\lambda) &= 1 - \lambda, & \forall \lambda \geq 0, & \quad (\text{ESQPT4}) \\
f_5(\lambda) &= -1 + \frac{1}{2\lambda} + \lambda, & \forall \lambda \geq \frac{3}{7}, & \\
f_6(\lambda) &= 1 - \frac{1}{2\lambda} - \lambda, & \forall \lambda \geq \frac{3}{7}, & \\
f_7(\lambda) &= 1 - \frac{5+\lambda^2}{10\lambda}, & \forall \lambda \geq \frac{1}{11}(10 - 3\sqrt{5}), & \\
f_8(\lambda) &= \frac{(1-3\lambda)^2}{8\lambda}, & \forall \lambda \geq \frac{1}{17}(7 - 4\sqrt{2}), & \\
f_9(\lambda) &= 1 - \frac{1}{2\lambda} - \frac{7\lambda}{6}, & \forall \lambda \geq \frac{3}{5}, & \\
f_{10}(\lambda) &= 1 - \frac{3+\lambda^2}{6\lambda}, & \forall \lambda \geq \frac{1}{7}(6 - \sqrt{15}), & \\
f_{11}(\lambda) &= \frac{(1+\lambda)^2}{10\lambda}, & \forall \lambda \geq \frac{1}{11}(4 - \sqrt{5}), & \\
f_{12}(\lambda) &= 0, & \forall \lambda \geq 0, & \\
f_{13}(\lambda) &= -\frac{(1-3\lambda)^2}{8\lambda}, & \forall \lambda \geq \frac{1}{17}(7 - 4\sqrt{2}), & \\
f_{14}(\lambda) &= \frac{(1+\lambda)^2}{8\lambda}, & \forall \lambda \geq \frac{1}{3}. &
\end{aligned} \tag{B2}$$

REFERENCES

- [1] H. Stanley, *Introduction to phase transitions and critical phenomena*, International series of monographs on physics (Oxford University Press, 1987).
- [2] H. Nishimori and G. Ortiz, *Elements of phase transitions and critical phenomena* (Oxford University Press, 2010).
- [3] S. Sachdev, *Quantum phase transitions* (Cambridge University Press, Cambridge, 2011).
- [4] M. Vojta, Quantum phase transitions, Rep. Prog. Phys. **66**, 2069 (2003).
- [5] L. Carr, *Understanding quantum phase transitions*, Condensed Matter Physics (CRC Press, 2010).
- [6] P. Cejnar, P. Stránský, M. Macek, and M. Kloc, Excited-state quantum phase transitions, Journal of Physics A: Mathematical and Theoretical **54**, 133001 (2021).
- [7] P. Stránský, M. Macek, and P. Cejnar, Excited-state quantum phase transitions in systems with two degrees of freedom: Level density, level dynamics, thermal properties, Annals of Physics **345**, 73 (2014).
- [8] M. Macek, P. Stránský, A. Leviatan, and P. Cejnar, Excited-state quantum phase transitions in systems with two degrees of freedom. iii. interacting boson systems, Phys. Rev. C **99**, 064323 (2019).
- [9] J. Khalouf-Rivera, J. Gamito, F. Pérez-Bernal, J. M. Arias, and P. Pérez-Fernández, Excited-state quantum phase transitions in the anharmonic Lipkin-Meshkov-Glick model: Dynamical aspects, Phys. Rev. E **107**, 064134 (2023).
- [10] J. Gamito, J. Khalouf-Rivera, J. M. Arias, P. Pérez-Fernández, and F. Pérez-Bernal, Excited-state quantum phase transitions in the anharmonic Lipkin-Meshkov-Glick model: Static aspects, Phys. Rev. E **106**, 044125 (2022).
- [11] P. Pérez-Fernández, P. Cejnar, J. M. Arias, J. Dukelsky, J. E. García-Ramos, and A. Relaño, Quantum quench influenced by an excited-state phase transition, Phys. Rev. A **83**, 033802 (2011).
- [12] D. J. Nader, C. A. González-Rodríguez, and S. Lerma-Hernández, Avoided crossings and dynamical tunneling close to excited-state quantum phase transitions, Phys. Rev. E **104**, 064116 (2021).
- [13] P. Pérez-Fernández, A. Relaño, J. M. Arias, P. Cejnar, J. Dukelsky, and J. E. García-Ramos, Excited-state phase transition and onset of chaos in quantum optical models, Phys. Rev. E **83**, 046208 (2011).
- [14] Y. Zhang, Y. Zuo, F. Pan, and J. P. Draayer, Excited-state quantum phase transitions in the interacting boson model: Spectral characteristics of 0^+ states and effective order parameter, Phys. Rev. C **93**, 044302 (2016).
- [15] H. J. Lipkin, N. Meshkov, and A. J. Glick, Validity of many-body approximation methods for a solvable model. (I). Exact solutions and perturbation theory, Nuclear Physics **62**, 188–198 (1965).
- [16] H. J. Lipkin, N. Meshkov, and A. J. Glick, Validity of many-body approximation methods for a solvable model: (III). Diagram summations, Nuclear Physics **62**, 211–224 (1965).
- [17] D. C. Meredith, S. E. Koonin, and M. R. Zirnbauer, Quantum chaos in a schematic shell model, Phys. Rev. A **37**, 3499–3513 (1988).
- [18] S. Gnutzmann, F. Haake, and M. Kuš, Quantum chaos of SU(3) observables, Journal of Physics A: Mathematical and General **33**, 143 (1999).
- [19] H.-J. Stöckmann, *Quantum Chaos: An Introduction* (Cambridge University Press, 1999).
- [20] H. Goldstein, C. Poole, and J. Safko, *Classical Mechanics* (Addison Wesley, 2002).
- [21] A. Peres, New conserved quantities and test for regular spectra, Phys. Rev. Lett. **53**, 1711 (1984).
- [22] M. Rautenberg and M. Gärttner, Classical and quantum chaos in a three-mode bosonic system, Phys. Rev. A **101**, 053604 (2020).
- [23] S. Kullback and R. A. Leibler, On information and sufficiency, Annals of Mathematical Statistics **22**, 79 (1951).
- [24] O. Castaños, R. López-Peña, J. G. Hirsch, and E. López-Moreno, Classical and quantum phase transitions in the Lipkin-Meshkov-Glick model, Phys. Rev. B **74**, 104118 (2006).
- [25] E. Romera, M. Calixto, and O. Castaños, Phase space analysis of first-, second- and third-order quantum phase transitions in the Lipkin–Meshkov–Glick model, Physica Scripta **89**, 095103 (2014).
- [26] D. Lacroix, Density matrix functional theory for the Lipkin model, Phys. Rev. C **79**, 014301 (2009).
- [27] E. Duzzioni and J. Marinelli, The two-level Lipkin model solution within the RPA approach for deformed fermions, Physics Letters A **326**, 322 (2004).
- [28] S. Baid, A. Sáiz, L. Lamata, P. Pérez-Fernández, A. M. Romero, A. Rios, J. M. Arias, and J. E. García-Ramos, Extended Lipkin model: Proposal for implementation in a quantum platform and machine learning analysis of its phase diagram, Phys. Rev. C **110**, 044318 (2024).
- [29] C. A. Bishop, M. S. Byrd, and L.-A. Wu, Casimir invariants for systems undergoing collective motion, Phys. Rev. A **83**, 062327 (2011).
- [30] J. Rai, C. L. Mehta, and N. Mukunda, Correlated states and collective transition operators for multilevel atomic systems. I, Journal of Mathematical Physics **29**, 510 (1988).
- [31] M. T. López-Arias and V. R. Manfredi, Wave function behaviours of the three-level Lipkin-Meshkov-Glick model, Zeitschrift für Physik A Atomic Nuclei **334**, 255 (1989).

- [32] S. Gnutzmann and M. Kuś, Coherent states and the classical limit on irreducible $SU(3)$ representations, *Journal of Physics A: Mathematical and General* **31**, 9871 (1999).
- [33] W.-G. Wang, F. M. Izrailev, and G. Casati, Structure of eigenstates and local spectral density of states: A three-orbital schematic shell model, *Phys. Rev. E* **57**, 323–339 (1998).
- [34] P. Leboeuf and M. Saraceno, Eigenfunctions of non-integrable systems in generalised phase spaces, *Journal of Physics A: Mathematical and General* **23**, 1745 (1999).
- [35] M. Calixto, A. Mayorgas, and J. Guerrero, Role of mixed permutation symmetry sectors in the thermodynamic limit of critical three-level Lipkin-Meshkov-Glick atom models, *Phys. Rev. E* **103**, 012116 (2021).
- [36] A. Barut and R. Raczka, *Theory of Group Representations and Applications* (Polish Scientific Publishers, Warszawa, 1980).
- [37] A. Mayorgas, Eigenenergies and eigenvectors of the 3-level Lipkin-Meshkov-Glick model symmetric representation for $N=100$ particles, *Zenodo* (2026).
- [38] P. Stránský and P. Cejnar, Classification of excited-state quantum phase transitions for arbitrary number of degrees of freedom, *Physics Letters A* **380**, 2637–2643 (2016).
- [39] C. M. Lóbez and A. Relaño, Entropy, chaos, and excited-state quantum phase transitions in the Dicke model, *Phys. Rev. E* **94**, 012140 (2016).
- [40] M. Caprio, P. Cejnar, and F. Iachello, Excited state quantum phase transitions in many-body systems, *Annals of Physics* **323**, 1106 (2008).
- [41] P. Cejnar and P. Stránský, Impact of quantum phase transitions on excited-level dynamics, *Phys. Rev. E* **78**, 031130 (2008).
- [42] I. García-Mata, M. A. P. Reynoso, R. G. Cortiñas, J. Chávez-Carlos, V. S. Batista, L. F. Santos, and D. A. Wisniacki, Impact of chaos on the excited-state quantum phase transition of the Kerr parametric oscillator, *Phys. Rev. A* **111**, L031502 (2025).
- [43] A. Mayorgas, Poincaré Sections of the 3-level Lipkin-Meshkov-Glick model in the mean field limit, *Zenodo* (2026).
- [44] F. Haake, S. Gnutzmann, and M. Kuś, *Quantum Signatures of Chaos*, 4th ed. (Springer Cham, 2019).
- [45] M. A. Stephens, Edf statistics for goodness of fit and some comparisons, *Journal of the American Statistical Association* **69**, 730 (1974).
- [46] J. E. García-Ramos, P. Pérez-Fernández, and J. M. Arias, Excited-state quantum phase transitions in a two-fluid Lipkin model, *Phys. Rev. C* **95**, 054326 (2017).
- [47] C. W. J. Beenakker, J. M. Edge, J. P. Dahlhaus, D. I. Pikulin, S. Mi, and M. Wimmer, Wigner-Poisson statistics of topological transitions in a Josephson junction, *Phys. Rev. Lett.* **111**, 037001 (2013).
- [48] M. Calixto, A. Mayorgas, and J. Guerrero, Lieb-Mattis ordering theorem of electronic energy levels in the thermodynamic limit, *Phys. Rev. E* **112**, 034125 (2025).
- [49] A. del Rio-Lima, F. J. Poveda-Cuevas, and O. Castaños, Entanglement of a three-level atom interacting with two-modes field in a cavity, *Journal of Physics B: Atomic, Molecular and Optical Physics* **57**, 185001 (2024).
- [50] M. Algarni, K. Berrada, S. Abdel-Khalek, and H. Eleuch, Three-level atom-field in the context of time-dependent coupling and power-lower potentials, *Results in Physics* **43**, 106089 (2022).
- [51] M. A. Bastarrachea-Magnani, S. Lerma-Hernández, and J. G. Hirsch, Comparative quantum and semiclassical analysis of atom-field systems. I. Density of states and excited-state quantum phase transitions, *Phys. Rev. A* **89**, 032101 (2014).
- [52] M. A. Bastarrachea-Magnani, S. Lerma-Hernández, and J. G. Hirsch, Comparative quantum and semiclassical analysis of atom-field systems. II. Chaos and regularity, *Phys. Rev. A* **89**, 032102 (2014).
- [53] J. E. García-Ramos, J. Dukelsky, P. Pérez-Fernández, and J. M. Arias, Phase diagram of an extended Agassi model, *Phys. Rev. C* **97**, 054303 (2018).
- [54] J. E. García-Ramos, J. Dukelsky, P. Pérez-Fernández, and J. Arias, An extended Agassi model: algebraic structure, phase diagram, and large size limit, *Physica Scripta* **94**, 044003 (2019).
- [55] J. Cerrillo, S. Oviedo Casado, and J. Prior, Low Field Nano-NMR via Three-Level System Control, *Phys. Rev. Lett.* **126**, 220402 (2021).
- [56] A. López-García and J. Cerrillo, Full qubit control of the double quantum transition in NV centers for low-field or high-frequency sensing, *EPJ Quantum Technology* **12**, 52 (2025).
- [57] S. Cao, W. Zhang, J. Tilly, A. Agarwal, M. Bakr, G. Campanaro, S. D. Fasciati, J. Wills, B. Shteynas, V. Chidambaram, P. Leek, and I. Rungger, Encoding optimization for quantum machine learning demonstrated on a superconducting transmon qutrit, *Quantum Science and Technology* **9**, 045037 (2024).
- [58] P. Gokhale, J. M. Baker, C. Duckering, F. T. Chong, N. C. Brown, and K. R. Brown, Extending the frontier of quantum computers with qutrits, *IEEE Micro* **40**, 64 (2020).
- [59] E. Acar and İhsan Yılmaz, Unlocking the high dimensional potential: Comparative analysis of qubits and qutrits in variational quantum neural networks, *Neurocomputing* **623**, 129404 (2025).
- [60] G. Bottrill, *Exploring trade-offs in quantum optimization with noisy qutrits*, Ph.D. thesis, University of British Columbia (2025).
- [61] A. Perelomov, *Generalized Coherent States and their Applications* (Springer-Verlag Berlin Heidelberg, 1986).
- [62] J. M. Radcliffe, Some properties of coherent spin states, *Journal of Physics A: General Physics* **4**, 313–323 (1971).
- [63] F. T. Arecchi, E. Courtens, R. Gilmore, and H. Thomas, Atomic coherent states in quantum optics, *Phys. Rev. A* **6**, 2211–2237 (1972).
- [64] M. Calixto, A. Mayorgas, and J. Guerrero, Entanglement and $U(D)$ -spin squeezing in symmetric multi-qudit systems and applications to quantum phase transitions in Lipkin-Meshkov-Glick D -level atom models, *Quantum Information Processing* **20**, 304 (2021).
- [65] I. Bengtsson and K. Życzkowski, *Geometry of Quantum States: An Introduction to Quantum Entanglement* (Cambridge University Press, 2006).